Investigation of Fatigue Properties and Interfacial Strengthening Mechanism in Al/Cu Bimetallic Lap Joints through Electromagnetic Pulse Welding

Yunqi Yan , Xinwei She * , Yang Ran , He Peng , Ruihao Zhang , Puquan Wang * , Xianquan Jiang *

Posted Date: 5 February 2024

doi: 10.20944/preprints202402.0246.v1

Keywords: Electromagnetic pulse welding; Al/Cu dissimilar joint; Fatigue resistance; Interfacial strengthening mechanism; Nanocrystalline Al2Cu

 doi:10.20944/preprints202402.0246.v1

Article

Investigation of Fatigue Properties and Interfacial Strengthening Mechanism in Al/Cu Bimetallic Lap Joints through Electromagnetic Pulse Welding

Yunqi Yan [1], Xinwei She [2,*], Yang Ran [3], He Peng [4], Ruihao Zhang [4], Puquan Wang [5,*] and Xianquan Jiang [4,*]

[1] Department of Mechanical and Engineering, Sichuan University of Science and Engineering, Huixing Road 519, Zigong 643000, China; 15808204693@163.com (Y.Y.)
[2] College of Materials Science and Engineering, Chong qing University of Technology, Chongqing 400054, China
[3] Institute of Optics and Mechanics, Chongqing Academy of Science and Technology, Yangliu Road 2, Chongqing 401123, China; forestchn@aliyun.com (Y.R.)
[4] Southwest University, Tiansheng Road 2, Beibei District, Chongqing 400715, China; penghe@swu.edu.cn (H.P.); 302644961@qq.com (R. Z.)
[5] Center for Joint Surgery, The First Affiliated Hospital, Army Medical University, Chongqing 400038, P. R. China.
* Correspondence: sxw1991@cqut.edu.cn (X.S.); 13698250260@163.com (P.W.); jsq89@swu.edu.cn (X.J.); Tel.: +86-13983073429 (X.S.); +86-13308349982 (P.W.)

Abstract: This study investigated the fatigue properties and interfacial strengthening mechanisms of Al6061-to-Cu dissimilar welded joints via electromagnetic pulse welding (EMPW). The load-bearing capacity of the joints at discharge voltages of 14 kV and 16 kV was superior to that of 12 kV. Meanwhile, the fatigue life of 14 kV joints was one order of magnitude higher than that of 12 kV. The SEM observation on the fatigue fracture surface shows that the typical "tire-mark" fatigue striation just appeared on the 14 kV joint, indicating higher ductility for handling more extended plastic deformation. The high EBSD acquisition was achieved except for the transition zone due to the formation of ultra-fine nanocrystalline Al_2Cu phase and amorphous phase, along with many dislocations. Dense low-angle grain boundaries (LAGBs) and refined grains formed along the bonding interface. This indicates that severe plastic deformation induced dislocations to form the substructure in such an instant (40-60 μs) during the high-velocity collision. The interfacial strength is not only due to the continuous interfacial diffusion layer with a "wave-like" or "inverted hook-like" pattern but also benefits from refined grains along the interface and in the transition zone, as well as the hybrid amorphous-nanocrystalline microstructure, which strengthens the joint through increasing ductility induced by refined grains and regulating amorphous or nanocrystalline phases to affect the balance between strength and ductility of the Al/Cu joint.

Keywords: Electromagnetic pulse welding; Al/Cu dissimilar joint; Fatigue resistance; Interfacial strengthening mechanism; Nanocrystalline Al_2Cu

1. Introduction

The bonding strength of different materials has become a significant component of lightweight design to build light, affordable, and environmentally friendly constructions [1]. However, due to the differences in the astrophysical characteristics of incompatible materials, severe segregation, and the development of brittle intermetallic compounds (IMCs), it is difficult to create sound joints using traditional fusion welding procedures. For example, the presence of IMCs in the Al/Cu welding interface was frequently characterized by brittle fractures, such as Al_2Cu, AlCu, Al_4Cu_9, etc., resulting in meager interfacial bonding strength [2–4]. The high-velocity impact of solid-state welding, such as electromagnetic pulse welding (EMPW) [5], doesn't require any heat input and instantly completes

 doi:10.20944/preprints202402.0246.v1

the welding process (in approximately 40-60 μs), which could potentially overcome segregation and reduce or prevent the generation of IMCs, resulting in an effective solution for joining dissimilar materials or multi-materials used across various industries, such as in aerospace, automotive, and power generation sectors.

As a result of these advantages, the performance of EMPWed dissimilar joints has been increasingly promoted. Lee et al. [6] successfully welded SPCC-A6111 and found that the joint exhibited higher shear strength than the Al base metal. Manogaran et al. [7] developed a magnetic spot-welding method that achieved a maximum shear load of 1100 N for a single Al-Fe weld. Patra et al. [8] conducted torsion tests on copper-steel tubular joints, and the failure occurred in the copper base metal. The above studies achieved excellent joint strength, potentially higher than base metal. However, these tests were performed under quasistatic loading conditions. IMCs in the dissimilar weld can weaken the joint under the dynamic fatigue cyclic load, even though the weld performs well under static loading conditions [9]. To ensure safety and reliability in the aerospace, automotive, and power industries, it is crucial to investigate the fatigue properties of EMPWed dissimilar joints. However, few researchers have paid attention to the fatigue performance of dissimilar joints. Geng et al. [10] reported the fatigue fracture properties of EMPWed Al-Fe lap joints, indicating that the weld showed better fatigue resistance than the base metal under low-stress amplitude. Meanwhile, brittle and ductile fractures were observed on the fatigue fracture surface. While the effect of interfacial bonding characteristics on fatigue strength is unclear, it is an essential topic to study.

A few studies have been conducted on investigations of EBSD (electron backscatter diffraction). Yvell et al. [11] observed the microstructure development in a high-nickel austenitic stainless steel. The evolution of low and high-angle boundaries and the orientation changes within individual grains were studied. To better understand the interface connection mechanism of Cu/Al joints produced by high-power ultrasonic welding (HUSW), Liu et al. [12] systematically investigated the intermetallic compounds and texture at the interface. Liyakat et al. [13] also investigated the microstructural characterization of the friction stir process (FSP) on the weld bead of Tungsten Inert Gas (TIG) welded 5052-H32 aluminum alloy using EBSD. However, there is a lack of systematical EBSD analysis for the interface characterization of EMPWed Al/Cu joint. In addition, Lee et al. [14] and Chen et al. [15] studied microstructure evolution using EBSD. However, TEM observations should further characterize the combination of crystalline and amorphous phases or the distribution of precipitates. Lee et al. [6] also found evidence of the potential presence of the amorphous phase in the transition layer at the EMPWed Al/Fe interface. Meanwhile, the TEM observations and diffraction patterns showed fine aluminum and Al-Fe intermetallic grains within the transition layer. Raoelison et al. [16] suggested that the formation of an amorphous phase at the interface resulted from localized melting followed by rapid solidification, raising questions about the interface morphology, melting, and their roles in bonding. However, the fine-grained and amorphous phase strengthening at the interfaces is still unclear and needs further exploration.

The present study was, therefore, aimed to investigate the fatigue properties of EMPWed Al/Cu dissimilar lap joints at different discharge voltages, examine the interfacial characteristics such as grain size and boundaries, texture, and crystallographic orientation, etc., through EBSD, identify the phase composition of the interface, and demonstrate the potential interface strengthening mechanism.

2. Materials and Methods

2.1. Materials and Welding Process

The commercial 6061-O Al alloy sheets and oxygen-free pure (99.9 wt.%) copper-T2 (equivalent to UNS C11000) sheets were used in the EMPW tests. The chemical compositions of both materials are listed in Tables 1 and 2. The Al and Cu sheets of 1 mm in thickness were machined into coupons of dimensions of 20 mm × 100 mm, with the length being parallel to the rolling direction. All the sheet surfaces were cleaned with ethanol, then dried before welding, being free of indentation, scratch, oil, burr, and other defects.

 doi:10.20944/preprints202402.0246.v1

Table 1. Chemical composition (wt.%) of the 6061-O Al alloy.

Material	Mg	Si	Cu	Mn	Fe	Zn	Ti	Cr	Ni	Al
6061 O-Al alloy	1.0	0.7	0.3	0.15	0.2	0.25	0.03	0.15	0.05	Bal

Table 2. Chemical composition (wt.%) of Cu-T2.

Material	Bi	Sb	As	Fe	Pb	S	Cu
Copper T2	0.001	0.002	0.002	0.005	0.005	0.005	≥99.90

Note: T2 copper is a Chinese designation for electrolytic tough pitch (ETP) copper, equivalent to UNS C11000 copper.

According to the rated power and properties of the equipment, the welding parameters of discharge voltages of U = 12 kV, 14 kV, and 16 kV with an initial gap of g = 1 mm were chosen to make the Al/Cu lap welded joints. A Pulsar electromagnetic pulse welding system (Figure 1a) of 70 kJ capacity (Chongqing Pulsa Technology Co. Ltd., Chongqing, China) along with an E-shaped one-turn flat coil actuator covered by insulator was utilized to perform EMPW of the Al/Cu samples. The initial gap between sheets is adjusted by changing the spacer height during the assembly and fixing processes of Al and Cu sheets, as sequentially exhibited in Figure 1b,c. Based on the principle of electromagnetic induction, as schematically illustrated in Figure 1c, when the capacitor (C) is charged, and then the discharge switch (G) is closed, a Lorentz force generated by the interaction of eddy current and magnetic field drives the flying sheet (Al sheet) hitting to the parent sheet (Cu sheet) with a high velocity to form Al/Cu lap welded joint.

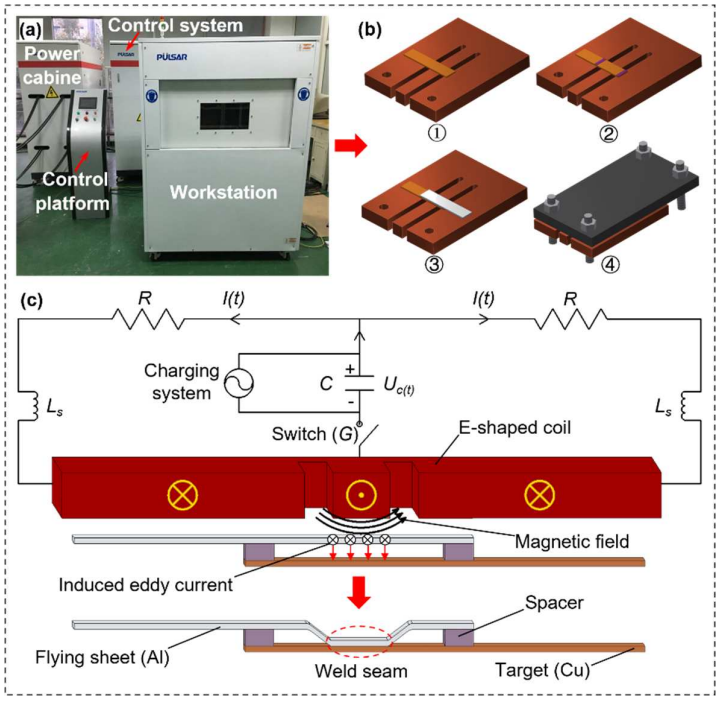

Figure 1. (a) Electromagnetic pulse welding (EMPW) system; The schematic diagram of (b) assembly and fixing processes of Al and Cu sheets, and (c) principle and process of EMPWed Al-Cu dissimilar alloys joint.

2.2. Mechanical Tests and Microstructure Characterization

After welding, the EMPWed Al/Cu joints for the mechanical test have a total length of 160 mm with an overlap of 40 mm, forming an annular weld zone and a non-weld zone (Figure 2a). Tensile lap shear tests were performed on five equivalent samples of each voltage using a fully computerized

 doi:10.20944/preprints202402.0246.v1

united testing machine at a constant crosshead speed of 1 mm/min at room temperature to acquire the maximum failure load. Furthermore, Load-control fatigue tests by ASTM E466-15 on a fully computerized Instron8801 servo-hydraulic testing system (Instron, Norwood, MA, USA) were conducted to investigate failure mode and fracture behavior of EMPWed Al/Cu dissimilar lap welded joints at different maximum cyclic loads. To avoid potential buckling of the test specimens, tension-tension cyclic loading at a stress ratio of R (P_{min} / P_{max}) = 0.2 was applied at 50 Hz with a sinusoidal waveform. Based on the results of interfacial failure, the selected fatigue fracture surface was examined via scanning electron microscopy (SEM, JEOL JSM-6480LV, JEOL, Tokyo, Japan) equipped with energy-dispersive X-ray spectroscopy (EDS).

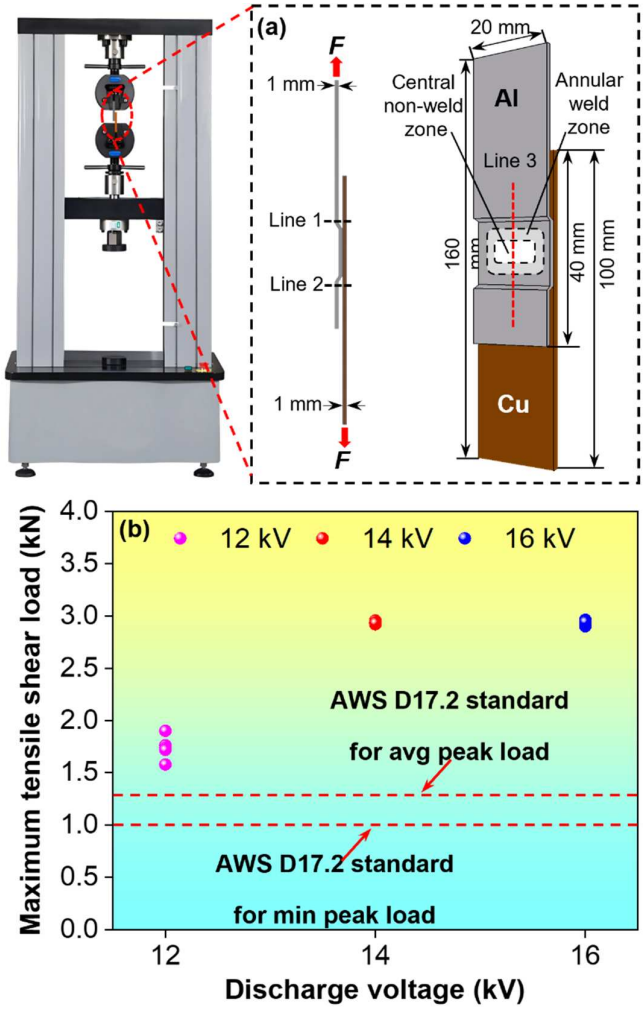

Figure 2. Tensile lap shear tests of EMPWed Al-Cu dissimilar alloys joint. (a) The schematic diagram of the test machine and the dimensions of the Al-Cu specimen, displaying the weld and non-weld zones along with the cutting line for the cross-section, (b) the maximum failure loads obtained in the tensile lap shear tests.

The EMPWed samples for electron backscattered diffraction (EBSD) examinations were prepared from the welded joints (sectioned along lines 1, 2, and then line 1, as shown in Figure 2a) using a slow-speed diamond cutter, then the sample surfaces were initially ground using emery papers, followed by mechanical pre-polishing using the diamond paste and colloidal silica suspension, and finally polished by an argon ion polishing equipment (Gantan 697) to eliminate the residual stress from previous processing steps, with a voltage of 7 kV and ion gun tilt angle of 1° for 20 min, then subsequently reducing the voltage to 5 kV for 10 min, 1 kV for 20 min, and 0.5 kV for 20 min, respectively. EBSD analyses were carried out using the SEM (ZEISS GeminiSEM 300) equipment

 doi:10.20944/preprints202402.0246.v1

with an Oxford-integrated Aztec HKL advanced EBSD system. An acceleration voltage of 20 kV, a working distance of 14.2 mm, and a sample tilt angle of 70° were selected for acquiring the data. For clear images and further detailed analyses, the overall interfacial bonding area and three interfacial transition zones containing insufficient grains were selected and scanned with a smaller step size of 0.08-0.5 um to ensure statistical significance. Additionally, T-EBSD (TKD, Transmission kikuchi diffraction) was performed to focus on the interfacial transition zone examination using SEM (ZEISS Gemini Sigma 500) at an acceleration voltage of 30 kV, a sample tilt angle of -20°, a working distance of 10 mm, and a fine step size of 0.02 um. Grain sizes, gain boundary misorientations, pole Figures, and other related microstructural features were acquired from EBSD data using the Aztec HKL Channel 5 and Azcrystal software. It should be noted that the welding direction (WD) is defined as parallel to the sheet rolling direction, the normal direction (ND) is defined as perpendicular to the welding direction, and the third direction is termed the welding tangent direction (TD). The TKD or TEM sample in this study was prepared using a dual-beam focused ion beam system (FIB, FEI Helios NanoLab 600i, FEI, USA). TEM observations were carried out using a Titan G2 60-300 (AC-TEM) super X microscope operating at 300 kV.

3. Results

3.1. Tensile Lap Shear Load

The schematic illustration of the tensile lap shear tests with the geometry and dimensions of EMPWed Al/Cu specimens is shown in Figure 2a. The diagram of maximum tensile lap shear loads at different discharge voltages is presented in Figure 2b, along with the specific values and various failure modes in Table 3. Since no standard for the tensile lap shear failure loads is available for EMPW thus far, the standard of AWS D17.2 [17] for the resistance spot welding is taken as a reference here, i.e., the two horizontal dashed lines indicating the lower (1.0 kN) minimum failure load and the higher (1.27 kN) average failure load plotted in Figure 2a based on a softer Al 6061-O sheet (Figure 2b) with a thickness of 1 mm. It is seen that the failure loads of the present EMPWed dissimilar joints at all three discharge voltages unanimously exceed the requirement specified in the AWS D17.2 standard. Specifically, all the 12 kV samples tested failed at the weld interface in an interfacial failure mode (IF). Despite this, the average failure load was 1741 N, exceeding the AWS D17.2 requirements. However, this interfacial failure mode suggests that the load-bearing capacity of the joint does not reach that of the Al and Cu base metals due to the absence of an adequate and continuous interfacial diffusion layer in our previous study [18]. On the other hand, all the 14 kV and 16 kV samples fracture in the Al base metal (BMF), implying that the load-bearing capacity of the joints at the discharge voltages is higher than that of Al base alloy, along with the average failure loads of 2935 N and 2939 N, respectively. These results suggest that well-bonded robust welding has been successfully achieved at 14 kV and 16 kV discharge voltages. Furthermore, the effect of the Al-Cu phase in the transition zone will be discussed in section 4.3. Consequently, it follows that the load-bearing capacity of the joints at both 14 kV and 16 kV is superior to that at 12 kV.

Table 3. Maximum tensile shear load and failure modes of EMPWed Al/Cu lap joints.

Discharge voltage (kV)	Maximum tensile shear load (N)	Failure mode
12	1764	IF
	1738	IF
	1902	IF
	1581	IF
	1721	IF
14	2939	BMF
	2926	BMF
	2957	BMF
	2921	BMF
	2934	BMF

 doi:10.20944/preprints202402.0246.v1

16	2963	BMF
	2936	BMF
	2902	BMF
	2951	BMF
	2944	BMF

3.2. Fatigue Behavior and Failure Mode

Fatigue tests under load control were conducted on EMPWed Al/Cu dissimilar lap welded joints, as shown in Figure 3a. Figure 3b illustrates the S-N curves of welded joints at 12 kV and 14 kV. Considering the experimental scatter during the dynamic fatigue tests, two samples were tested at each loading level. The maximum cyclic load P_{max} was applied from 0.5 kN to 3 kN with an interval of 0.5 kN based on the failure loads in Table 3, whereas the P_{max} = 3.0 kN was insufficiently applied at 12 kV due to fewer fatigue cycles at the loading level of P_{max} = 2.5 kN, i.e., approximately 29 and 26. The fatigue limit for the welded joints made at both voltages was 0.5 kN, which was deemed to have infinite fatigue life due to run-out data points for samples without failure beyond 1×10^7 cycles. It can be seen that the fatigue life of the joint made at a discharge voltage of 14 kV was higher than that of 12 kV at all loading levels except 0.5 kN with small dispersion and good stability, which was consistent with the tensile test results (Figure 2b). It was partly attributed to enhancing the load-bearing capacity, fracture ductility, and fatigue resistance of joint made at a discharge voltage of 14 kV. Furthermore, it is worth noting that the Al base metal failure only happened for the joints obtained under the discharge voltage of 14 kV and P_{max} = 3.0 kN load condition, which is less than the load-bearing limits of Al/Cu lap welded joint while more extensive than that of Al base metal, resulting in fast failure in Al base metal but less time to fatigue for the joint. However, as for other load conditions from 2.5 kN to 1 kN, just interfacial failure was observed. By this time, the Al base metal could resist these maximum loads. Therefore, Al/Cu lap joints underwent more progressive plastic deformation during fatigue. In addition, the applied load of 0.5 kN was too low to result in joint failure, exhibiting the most extended fatigue life. In a word, the enhanced fatigue life of the weld joint at 14 kV significantly correlates with the higher load-bearing capacity; thus, reasonably increasing the voltage is crucial in ensuring welding stability. Figure 3b and c show the failure mode in conjunction with the logarithmic S-N plots in the form of the maximum tensile shear cyclic stress vs the number of reversals to failure ($2N_f$) in terms of a Basquin-type relationship for EMPWed Al/Cu samples at discharge voltages of 14 kV and 12 kV. It can be seen that the run-out data for the non-failed samples at or over 1×10^7 cycles were not included in the curve fitting. For the weld joint made at 14 kV in Figure 3c, the BMF mode was observed at the highest P_{max} = 3.0 kN, while the IF mode occurs at other load conditions with a fatigue strength coefficient of 360 MPa and fatigue strength index of -0.2188. For the weld joint made at 12 kV in Figure 3c, only IF mode was acquired for all load conditions with a fatigue strength coefficient of 73 MPa and fatigue strength index of -0.1076, which agreed with their static strength. It is well known that the higher the value of fatigue strength exponent, the longer the fatigue life.

 doi:10.20944/preprints202402.0246.v1

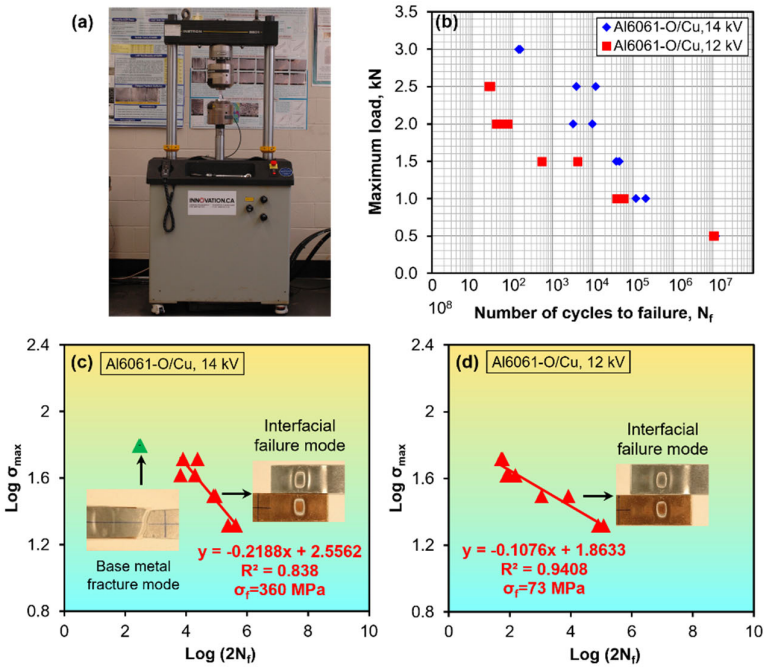

Figure 3. (a) Fatigue test machine, (b) S-N curves, and (c, d) the maximum tensile shear cyclic stress vs. the number of reversals to failure ($2N_f$) in the double-log scale for the EMPWed Al 6061-to-Cu dissimilar lap welded joint made at the parameters of 14 kV and 12 kV, respectively, and tested at RT, R = 0.2, and a frequency of 50 Hz, where different failure modes are indicated.

3.3. Fatigue Fractography

SEM observations on fatigue fracture surfaces were conducted to study the failure characteristics in detail during the crack initiation, propagation, and fast fracture processes. Figure 4 presents the images of the interfacially failed fatigue sample welded at the discharge voltages of 14 kV (Figure 4a–f) and 12 kV (Figure 4g–l) and tested at a lower cyclic load of P_{max} = 1 kN. Figure 4a shows an overall view of the fatigue fracture surface on the Cu side, along with four typical zones, i.e., zones A, B, C, and D, in the annular welding area. Figure 4b shows an enlarged view of zone A, illustrating fatigue crack developed from the outer edge of the annular welding area due to stress concentration resulting from the irregular shape margin and combination role of shear and normal stress during lap fatigue tests, then underwent fatigue crack propagation along stress gradient or load direction, where the applied stress intensity factor reached the fracture ductility value of the materials. Subsequently, fast cracks mainly featured dimples propagated toward the inner edge. This fatigue fracture phenomenon was discussed in detail in our previous work [19]. Figure 4c shows the fatigue and dimple features along the interface in zone E during the transition from fatigue fracture to fast fracture. Moreover, the fatigue crack growth zone characterized by the fatigue feature (Figure 4b) is relatively large in comparison with the fast crack growth zone, which implies a fatigue life primarily spent in the stage of crack propagation as a form of yielding and plastic deformation of the crack tip [20]. It is of interest to note in Figure 4d that some particular "tire-mark" fatigue striation occurred in zone B via a repeated plastic blunting-sharpening process within the plastic zone ahead of the fatigue crack tip under a couple roles of shear and normal stress, suggesting crack propagating along the welding circumference, which was also reported by Feng [21]. Figure 4e,f present the typical tensile and shear dimple in zone C, indicating the main opening load or shear stress led to the final fracture. Consequently, it could be understandable that the crack initiated from zone A and then propagated to the final fracture zone in zone D along the annular weld. A similar fatigue fracture mode was also reported by Geng [10]. As a comparison, Figure 4g exhibits a smaller annular welding area. Figure 4h shows a similar fracture mode to that in Figure 4b, with a slight fatigue feature (Figure 4i) and

 doi:10.20944/preprints202402.0246.v1

dimple feature (Figure 4j). In addition, Figure 4k presents inconspicuous fatigue striation in zone G, indicating the absence of fatigue load-bearing capacity compared to that in Figure 4d. At the same time, the tensile dimple almost featured the final fast fracture zone in Figure 4l.

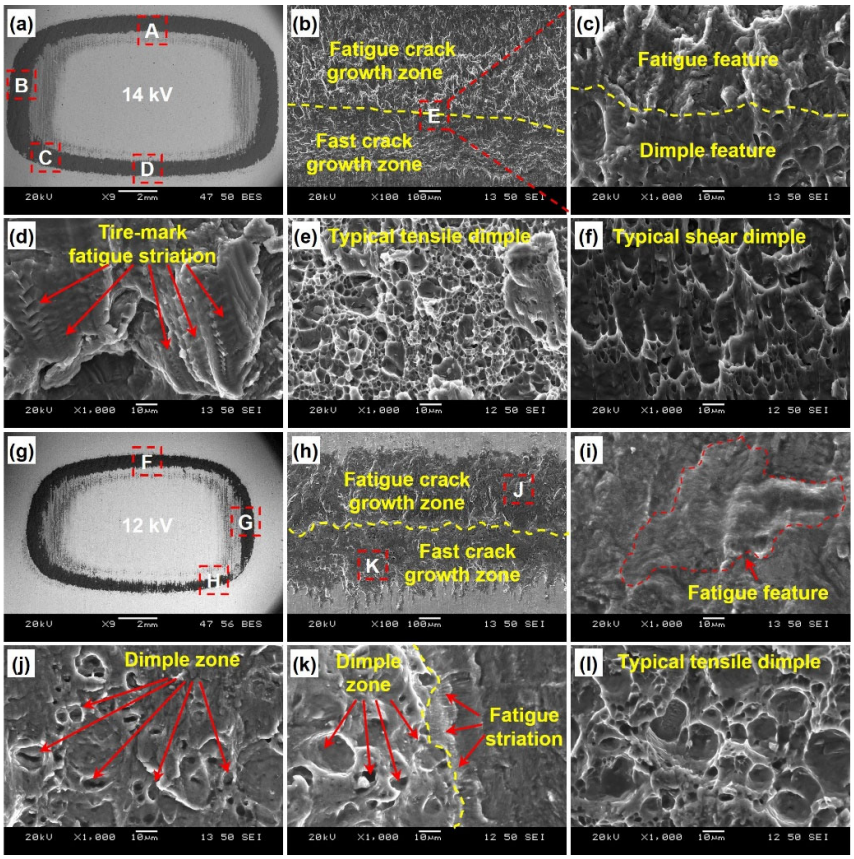

Figure 4. Typical SEM images of the fatigue fracture surface of a dissimilar EMPWed Al/Cu joint at the parameters of (a-f) U = 14 kV and (g-l) U = 12 kV and tested at a P_{max} 1.0 kN. (a) Overall view, (b) morphology of fatigue crack and fast fracture in zone A, (c) fatigue feature transfer to dimple in zone E, (d) tire-mark fatigue striation in zone B, (e, f) typical tensile dimple and shear dimple in zones C and D, respectively; (g) Overall view, (h) morphology of fatigue crack and fast fracture in zone F, (i, j) fatigue feature and dimple feature in zones J and K, respectively; (k) fatigue striation and dimple in zone G, (l) typical tensile dimple in zone H.

Figure 5 also presents the observation on fatigue fracture surfaces of the sample welded at the discharge voltages of 14 kV (Figure 5a–f) and 12 kV (Figure 5g–l) and tested at a higher cyclic load of P_{max} = 2.5 kN, sharing a similar fracture mode to that in Figure 4. The noteworthy difference is the smaller fast-fatigue crack growth zone in Figure 5b or even the only fast crack growth zone in Figure 5h. Since the shear stress dominated a primary factor and the fatigue strength is insufficient to resist the higher cyclic loading P_{max} = 2.5 kN to perform adequate propagation of fatigue crack, but still characterized by the successive "tire-mark" fatigue striation as indicated in Figure 5d and but absence in Figure 5j. Fatigue striations are more clearly visible in the samples that failed at lower cyclic loads than those failing at higher cyclic loads due to the reduced fatigue life [22]. The final fast fracture zone is characterized by shear or tensile dimple, as shown in Figure 5e,f,k,l. As a result, it could be concluded that the EMPWed Al/Cu dissimilar lap welded sample made at 14 kV performed a superior fatigue resistance than that at 12 kV, mainly attributed to the larger annular welding area and stronger interface bonding. Thus, the detailed interface bonding is well worth studying.

 doi:10.20944/preprints202402.0246.v1

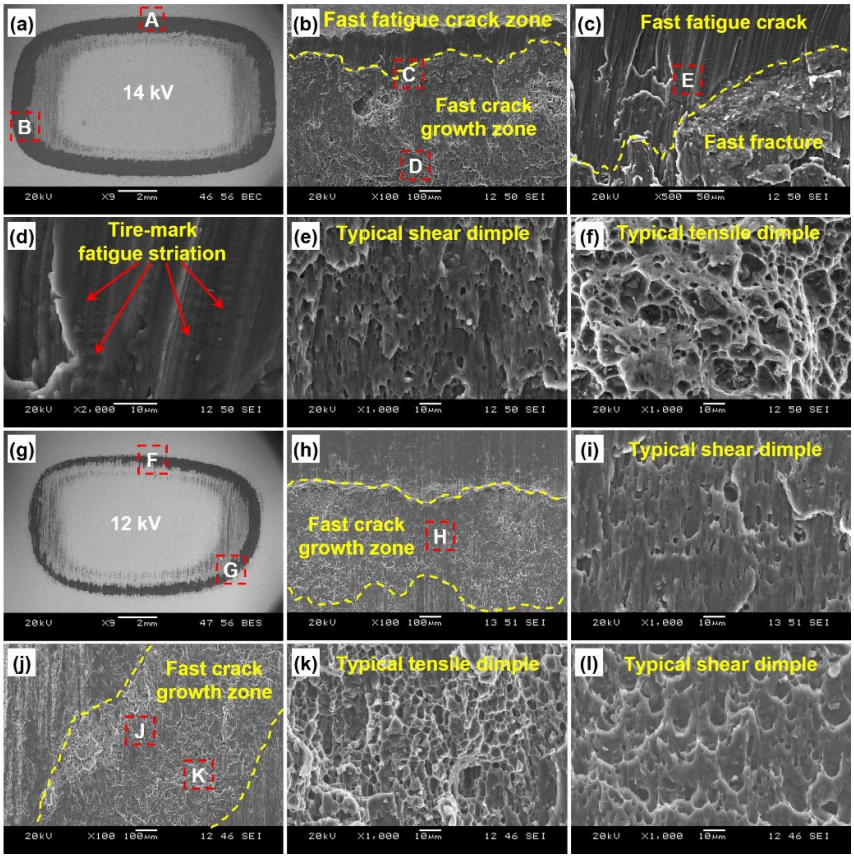

Figure 5. Typical SEM images of the fatigue fracture surface of an EMPWed Al/Cu dissimilar lap joint at the parameters of (a-f) U = 14 kV and (g-l) U = 12 kV and tested at a P_{max} 2.5 kN. (a) Overall view, (b) morphology of fast fatigue crack and fast fracture in zone A, (c) magnified image of zone C, (d) slight tire-mark fatigue striation in zone E, (e, f) typical shear and tensile dimple in zones D and B, respectively; (g) Overall view, (h) morphology of fast fracture in zone F, (i) typical shear dimple in zone H, (j) morphology of fast fracture in zone G, (k, l) typical tensile and shear dimple in zones J and K, respectively.

3.4. EBSD Analysis

Interface bonding performance was examined through EBSD detection on the sample welded at a discharge voltage of 16 kV due to excellent load-bearing capacity and rich interfacial bonding characteristics. During the EBSD analysis, grain boundaries with misorientation angles in the 2-15° range were defined as low-angle boundaries (LAGBs), and those exceeding 15° were assigned high-angle boundaries (HAGBs). The blue, green, deep red, and black and red lines in EBSD maps represented (1 1 1), (1 0 1), (0 0 1), HAGBs, and LAGBs, respectively. The present EBSD studies used normal-projected orientation maps, color legend, pole Figures (PFs), and inverse pole Figures (IPFs), i.e., the projection direction is normal to the TD and the observed surface. Figure 6a shows a schematic diagram of the weld zone for EBSD detection at an Al/Cu cross-sectional sample. Figure 6b displays the mean angular deviation (MAD) of grain boundaries, reflecting data acquisition quality with an excellent global resolution rate due to most of the MAD being lower than 1°. A large number of LAGBs filled the area around the interface on the Al side (Figure 6c), which can be attributed to the fact that the Al sheet collides with the Cu sheet at high speed, and the strong impact causes grain reconstruction, especially in the area near the interface. As seen in Figure 6d, the EBSD orientation map presented colorful grains, indicating a relatively weak or more random texture. Figure 6e–g shows the grain distribution satisfying with an average grain size lower than 100 μm, which can be seen that most of the small grains (D<25 μm) are concentrated near the interface, which happens to

 doi:10.20944/preprints202402.0246.v1

be the same region where LAGBs are enriched. Therefore, collision-refined grains and LAGBs are the interface's main features, which may contribute to improving joint strength.

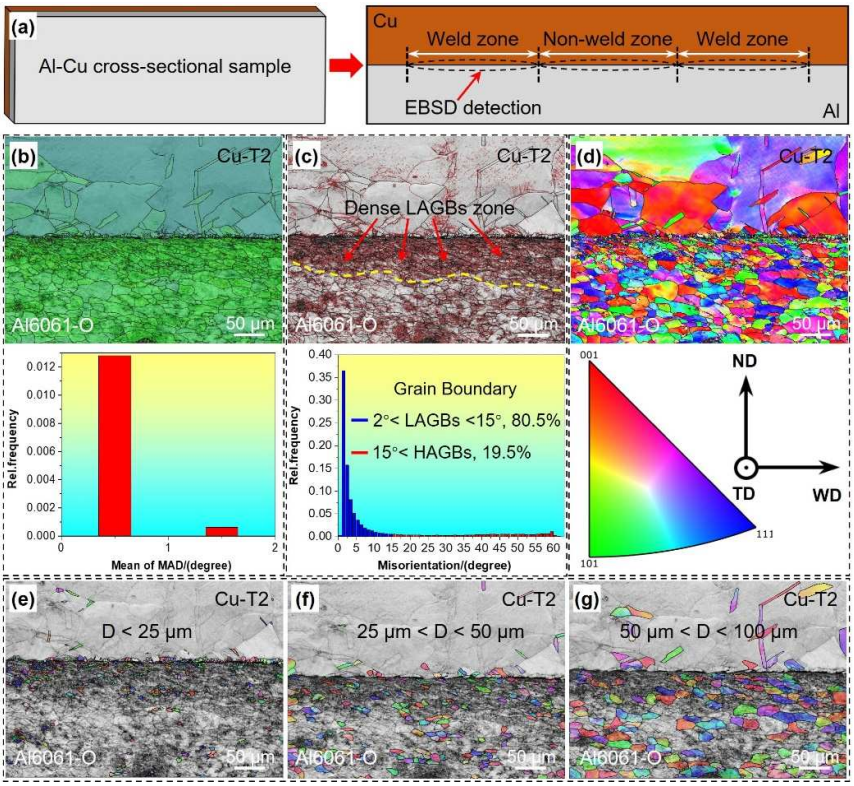

Figure 6. EBSD analysis of EMPWed Al/Cu joint at U = 16 kV. (a) The schematic diagram of Al-Cu EBSD sample with detection location, (b) mean angular deviation (MAD) map with acquisition data, (c) distribution of grain boundary misorientation, (d) EBSD orientation (IPF-Z) map, the grain size distribution of (d) D<25 μm, (e) 25 μm<D<50 μm, and (f) 50 μm<D<100 μm.

To identify the effect of the transition zone at the interface, zones I, II, and III, including wave-like or inverted hook-like diffusion layer, were re-scanned with a smaller step size of 0.08 μm, as shown in Figure 7a. As seen from the Figure 7b–d, the HAGBs and LAGBs of the three zones are more uniformly distributed near the transition zones. The grain size ranges from 0.29 μm to 13.7 μm. However, the diffusion layer is hard to resolve even at this precision. In the kernel average misorientation (KAM) map of Figure 7e, it can be observed that most areas of strain concentration coincide with LAGBs, which indicates that severe plastic deformation occurred during the grain reconstruction process, resulting in the formation of lots of LAGBs and strain concentration. Furthermore, Figure 7f exhibits the interfacial deformation situations, i.e., substructure area (yellow), deformation area (red), and the area of grain orientation difference angles less than 1° (blue), respectively. LAGBs are almost exclusively concentrated in the substructure region, indicating that collision-induced grain reconstruction produced most of the LAGBs and substructures. With sufficient energy, these substructures will fully crystallize, forming refined grains. As seen in Figure 7g, the TKD test was conducted with a much smaller step size of 0.02 μm to explore the diffusion layer. However, it was still unable to effectively detect and analyze the diffusion layer information, which could be concluded for three reasons: the grain size was less than 20 nm, resulting in invalid detection in existing precision; formation of amorphous; large deformation with stress concentration, meanwhile, the grain size ranges from 0.07 μm to 1.51 μm. Therefore, a detailed analysis of the transition zone requires TEM observation.

 doi:10.20944/preprints202402.0246.v1

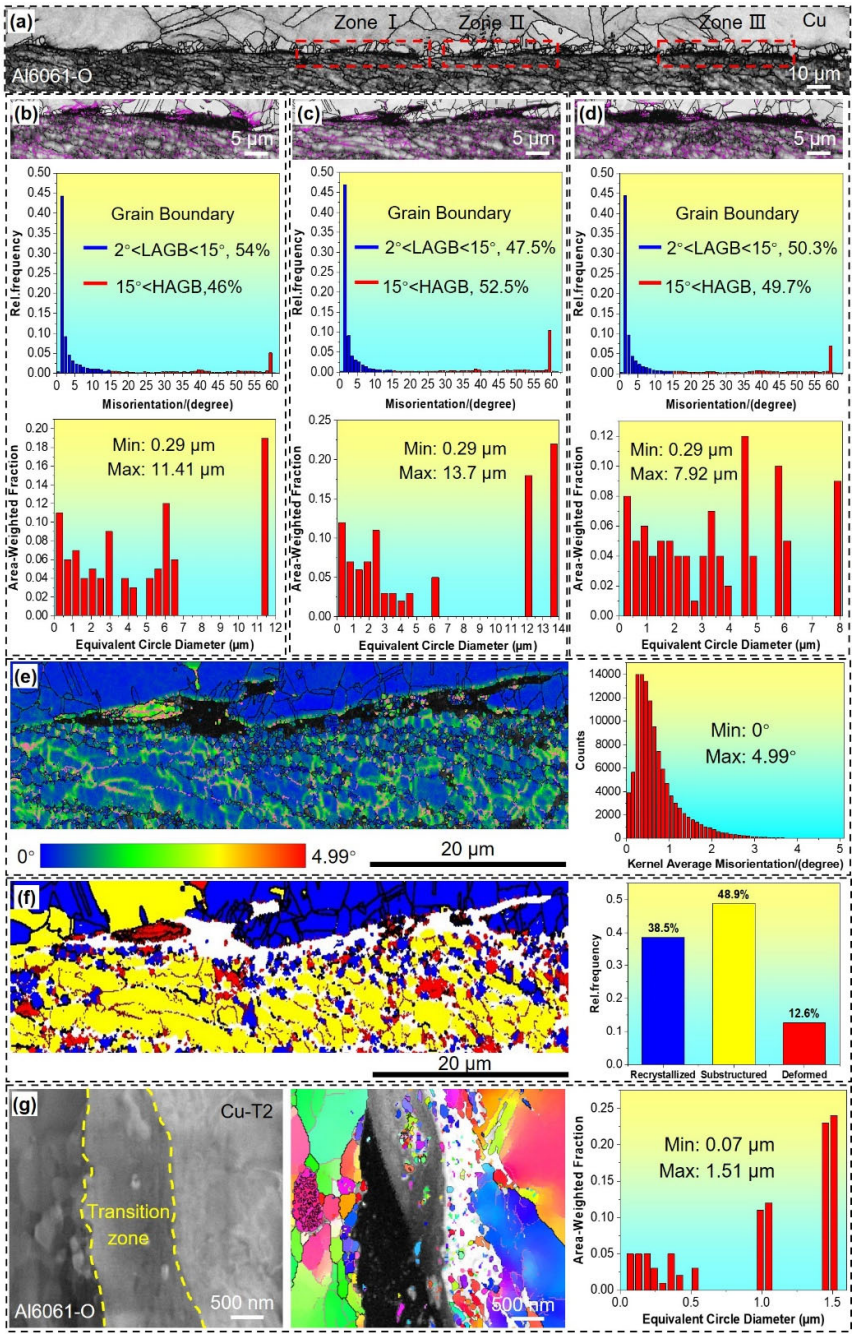

Figure 7. EBSD results at the interface of EMPWed Al/Cu joint at U = 16 kV. (a) Band contrast map with the interfacial characteristics indicated by red dashed box, (b-d) grain boundary misorientation and grain size distribution in (b) zone I, (c) zone II, and (d) zone III, (e, f) Kernel average misorientation and grain deformation of zone II, respectively; (g) Transmission kikuchi diffraction (TKD) result at the interface of EMPWed Al/Cu joint at U = 16 kV.

The EBSD orientation maps (IPF-X, IPF-Y, and IPF-Z parallel to WD, ND, and TD, respectively) of zone II along with their corresponding pole Figures (PFs), inverse pole Figures (IPFs), and orientation distribution function (ODF) are shown in Figure 8. Figure 8a and c shows that the grains along the interface tend to be colorful, indicating a relatively weak or more random texture. Figure 8b illustrates that the grains displayed colorfully on the Al side and mainly green on the Cu side, indicating the presence of a stronger < 1 0 1 > texture (Figure 8d). Further texture analysis showed

 doi:10.20944/preprints202402.0246.v1

that the corresponding (0 1 1) PFs and IPFs confirmed the orientation poles and < 1 0 1 > direction parallel to TD (Figure 8e). The overall three-dimensional Euler space diagram (Figure 8f) and sections (Figure 8g) of the orientation distribution function (ODF) signify the presence of a brass texture component with Euler angle {35, 45, 0} and its distribution along the interface (Figure 8h).

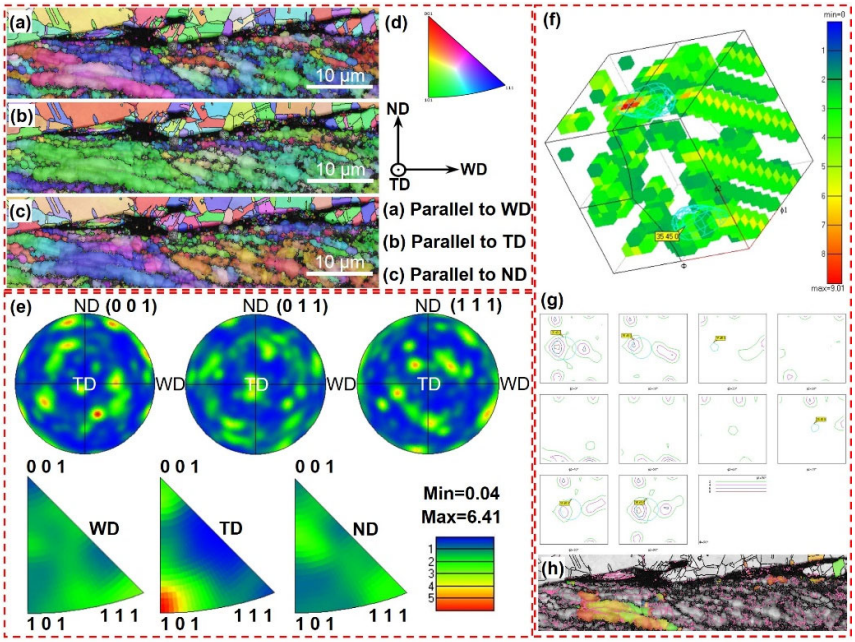

Figure 8. EBSD analysis along the interfacial characteristic in zone II in Figure 4a. Orientation maps of (a) IPF-RD, (b) IPF-TD, (c) IPF-ND, and (d) the legend with directional indicator; (e) the corresponding (0 0 1), (0 1 1), and (1 1 1) pole figure, inverse pole figure, respectively; (f, g) the corresponding ODF maps in 3D and 2D view, respectively, along with typical (35° 45° 0°) euler angles of brass texture; (h) the distribution of brass texture.

3.5. TEM Characterization

As seen in Figure 9, the TEM observation was conducted to examine the phase in the transition zone. Figure 9a presents the interfacial HAADF (annular high-angle dark-field) image of the EMPWed Al-Cu joint made at 16 kV. Smaller grains on the Al or Cu side and a distinct ultra-fine grain band between both sides can be seen. Figure 9b and c exhibited the enlarged view of zones A and B in Figure 9a, displaying the interface between the Al side and transition zone and the transition zone and Cu side, respectively. The existence of nano-scale grains in the transition zone is apparent. Figure 9d shows the HRTEM (High-resolution TEM) image of zone C in Figure 9a. The FFT (Fast Fourier transform) image (Figure 9e) presents a nano-polycrystalline diffraction ring, which was calibrated to be Al_2Cu with corresponding characteristic crystal planes, i.e., (1 1 0), (2 1 1), (2 2 0), and (2 2 1). They can also be found in Figure 9d, along with the spacing between related crystal planes. As seen in Figure 9f, the IFFT (Inverse fast Fourier transform) image of zone E exhibits a hybrid lattice stripe of disorder arrangement and long-ranged order, indicating the existence of an amorphous phase. Meanwhile, Figure 9g and h show numerous dislocations, probably caused by intense plastic deformation in localized zones F and G in Figure 9d during the high-velocity impact. In addition, the HRTEM image of another zone D in Figure 9a was also calibrated to be Al_2Cu with the same crystal planes as in Figure 9e and similar crystal plane spacing. Similarly, Figure 9k presents a hybrid lattice stripe of disorder arrangement and short-range order, further confirming the amorphous phase in zone H. Moreover, the presence of dislocations in zones J and K is also demonstrated in Figure 9m and n. In a word, during the high-velocity impact, nanocrystalline Al_2Cu was formed in the transition zone, accompanied by the formation of amorphous phases and dislocations in some local zones, which may be the reason why EBSD and TKD could not resolve the transition zone.

Preprints.org (www.preprints.org) | NOT PEER-REVIEWED | Posted: 5 February 2024 doi:10.20944/preprints202402.0246.v1

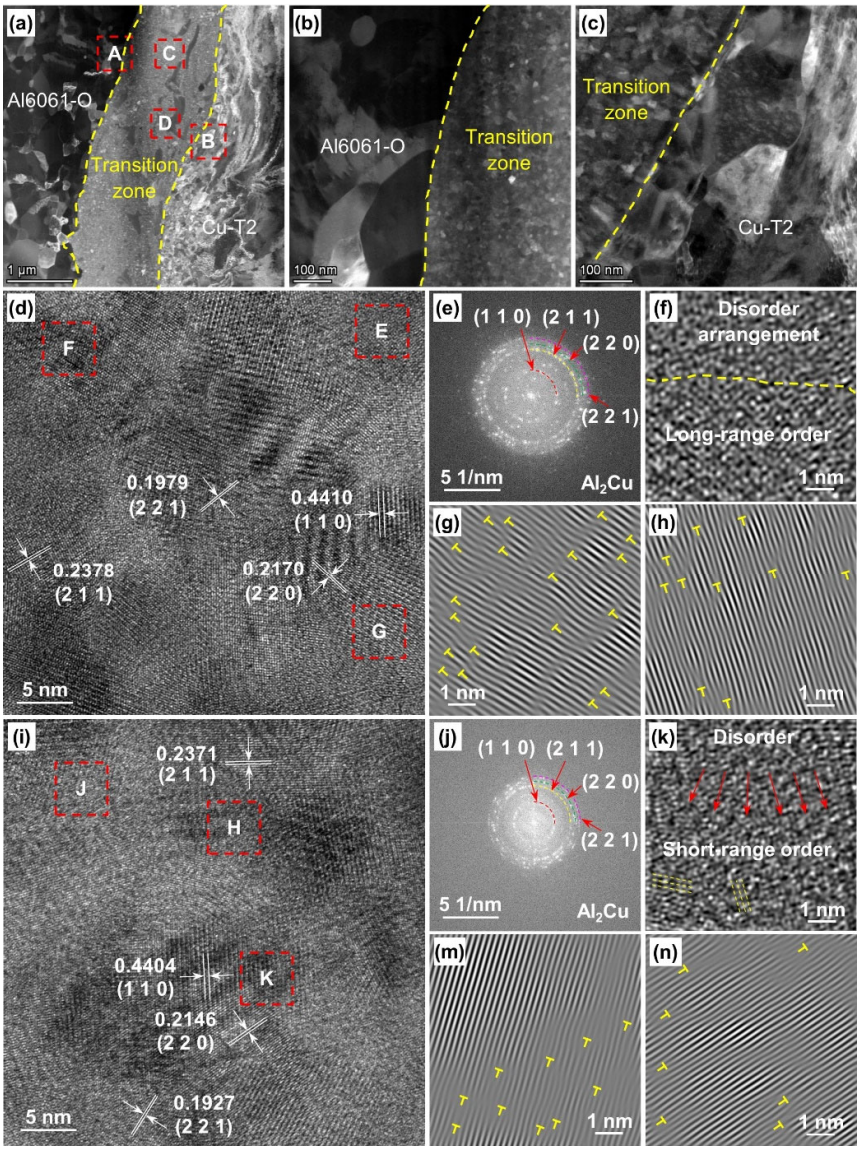

Figure 9. (a) HAADF image of the interface of EMPWed Al/Cu joint at U = 16 kV, (b, c) magnified images of zone A and zone B, respectively, (d) HRTEM image in zone C, with corresponding (e) FFT image, (f) IFFT image of zone E, and (g, h) dislocations in zones F and G; (i) HRTEM image in zone D, with corresponding (j) FFT image, (k) IFFT image of zone H, and (m, n) dislocations in zones J and K.

4. Discussion

4.1. Fatigue Properties

As mentioned in sections 3.1 and 3.2, the enhanced fatigue life is related to the joints' higher tensile lap shear loads since it is known that the load-controlled fatigue strength of a material is proportional to its tensile strength. As shown in Figure 3b, the fatigue cycles at 14 kV are one order of magnitude higher than that at 12 kV, especially in the case of P_{max} = 1 kN, the number of cycles for 12 kV specimens is in the order of 10^4, while that for 14 kV is 10^5, indicating that the specimens at both voltages are in the low-cycle fatigue and high-cycle fatigue [23], respectively. Furthermore, the dependence of the maximum cyclic load and number of reversals that lead to failure can be expressed by using the Basquin equation [24]:

 doi:10.20944/preprints202402.0246.v1

$$\sigma_a = \sigma_f (2N_f)^b \quad (1)$$

N_f is the number of fatigue cycles, σ_f is the fatigue strength coefficient, and b is the fatigue strength exponent. As seen from Figure 3c and d, when the fatigue strength coefficient is higher, and the fatigue strength index is lower, the fatigue life is longer, resulting in a more excellent fatigue resistance for the 14 kV specimen compared to that of 12 kV. Meanwhile, it is seen from Figure 3c that fast BMF occurred when the cyclic loads (3 kN) exceeded the yield strength of the Al base metal, indicating that the load-bearing capacity of the joint made at 14 kV could reach that of Al base metals. The improved fatigue life is attributable to the increase in the annular welding area with the increasing discharge voltage employed in the present study and the interfacial bonding mode, specifically the interlocking of wave-like or inverted hook-like diffusion layer at the interface [18].

The morphological characteristics on the fatigue fracture surface further indicate that the 14 kV joint has higher ductility than 12 kV and can withstand longer plastic deformation. As seen from Figures 4 and 5, the fatigue fracture mode on both voltages tends to be consistent, i.e., the stress concentration and fatigue crack initiated from the outer edge of the annular welding area until joint failure, which was attributed to a coupled role of shear and normal stresses present in a tensile lap shear sample due to the bending moment caused by the inherent misalignment [19]. Patel et al. [25] also reported that the nugget edge is a region of stress concentration in USWed joints with triaxial stresses, which can lead to transverse through-thickness crack growth failure. This generates a sufficient stress level of normal stress combined with the stress arising from the bending moment, ultimately leading to crack initiation, propagation perpendicularly to the loading direction, and eventually failure. However, when P_{max} = 1 kN, a distinct "tire-mark" fatigue appeared on the 14 kV joint (Figure 4d), while the 12 kV joint showed only slight fatigue feature (Figure 4i); when P_{max} = 2.5 kN, although the formation of fast fatigue fracture zone (Figure 5b,c), the "tire-mark" fatigue striation still existed in 14 kV joint (Figure 5d), but 12 kV only shown a fast fracture zone with dimples without fatigue striation. The typical characteristic of fatigue crack propagation is the presence of fatigue striation, such as distinct tire-mark fatigue striation (Figure 4d), slight fatigue feature (Figure 4i), and faint tire-mark fatigue striation (Figure 5d). Fatigue crack initiation is affected by various factors, such as surface finish, grain size, residual stress, environment, frequency of stress cycle, and temperature [26]. It is well known that the fatigue crack initially forms and propagates in a pure shear manner because of the direction of the maximum shear stress, while the growth rate is low. Subsequently, the continuous obstruction of grain boundaries causes the crack growth direction to become perpendicular to the load direction. The repeated plastic blunting-sharpening process within the plastic zone ahead of the fatigue crack tip under a couple of roles of shear and normal stress causes fatigue striation, suggesting that the 14 kV joint experienced more extended plastic deformation during the crack propagates along the welding circumference. Additionally, research conducted by Laird et al. [27] has demonstrated that the slip of dislocations caused the formation of fatigue striations at the crack tip in the plastic zone. Future investigations should concentrate on elucidating the formation mechanism of tire marks relating to grain refinement and grain slip.

4.2. Interfacial Characteristics

In the step size of 0.08-0.5 um, the acquisition quality of EBSD is higher except for the transition region (Figure 6b), this is due to the formation of ultra-fine nanocrystalline Al_2Cu phase and amorphous phase in the transition zone, which exceeds the detection limit. At the same time, there are many dislocations in the transition zone, indicating that it has undergone severe plastic deformation, which also leads to the failure of EBSD to collect data. Solid-state welding, such as explosive welding, friction stir welding, ultrasonic spot welding, electromagnetic pulse welding, and so on, is a process that uses physical actions such as pressure, collision, vibration, and friction to eliminate surface impurities to enable fresh contact surface atoms to be near each other, resulting in solid-phase bonding and a potential grain refinement at the interface. As seen in Figure 6e–g and Figure 7b,c,d,g, the high-velocity collision converts kinetic energy into plastic deformation work, which creates instantaneous high temperature and pressure at the interface, i.e., the high strain rate

 doi:10.20944/preprints202402.0246.v1

deformation led to interface grain refinement in the EMPWed joint. Despite different strain paths, this result is consistent with severe plastic deformation processes that lead to final equiaxed nano-crystalline structures [28]. A similarly fined microstructure was observed due to dynamic recrystallization resulting from the extreme temperatures and pressures in the regions nearest to the interface [29,30]. Meanwhile, explosive welding is also a short-cycle process, the grains exposed to a fast thermal cycle prevent their growth [31]. Liyakat et al. [32] reported a refinement of grain structure in the stir zone due to the influence of high stirring action, intense plastic deformation, and frictional heat during Friction Stir Processing (FSP).

The dense LAGBs zone was observed in Figure 6c, indicating severe plastic deformation on the Al side along the bonding interface. During the early stage of plastic deformation, stress concentration at the grain boundary leads to dislocation emission. When dislocation movement encounters a grain boundary, it becomes hindered by the potential barrier and becomes packed behind the grain boundary, gradually accumulating LAGBs. The interaction and entanglement of dislocations lead to the formation and evolution of LAGBs, which can be treated as a collection of dislocations, forming substructures and continuing the recovery and recrystallization process under certain conditions, such as heat treatment [33,34]. Lu et al. [35] and Liu et al. [36] proposed that accumulation of deformation heat and friction heat due to ultrasonic vibration acting on the joint reduces the driving force required for dislocation motion, and crystal defects such as dislocations and substructure nucleate and grow into the equiaxed grain, which rapidly grow or merge into larger grains with increased ultrasonic welding time. Gholinia et al. [37] also argued that the change process was geometrically dynamic recrystallization. However, the high-velocity collision of EMPW causes severe plastic deformation in an instant (40-60 μs), preventing sufficient time for active recovery and recrystallization. Hence, as the most severe plastic deformation occurred along the interface at the Al side, a dense interweaving of LAGBs was formed. The initiation, aggregation, and expansion of LAGBs can cause substructures (Figure 7f) and induce refined sub-grains (Figure 7b–d) that exacerbate the inhomogeneous deformation inside the grains. In the meantime, as shown in Figure 8, apart from the brass texture formed in the local area near the interface of the Al side, most of the area displayed a freedom texture during the short collision welding time.

4.3. Interfacial Strengthen Mechanism

As previously discussed, both EBSD and TEM analysis have revealed that the EMPWed Al/Cu lap joint not only features a continuous interfacial diffusion layer with a "wave-like" or "inverted hook-like" pattern but also benefits from fine-grain strengthening and amorphous-nanocrystalline hybrid strengthening, which should be further discussed. It's seen from Figure 6 that the grains along the interface at the Al side tend to have some degree of deformation and refinement under the high-velocity collision. Trueb et al. [38] also reported that grains near the mating interface of the MPW joint are extensively elongated along the welding direction due to the impact pressure. The effective refinement and elongation of grains can significantly influence hardening, which was supported by the literature [39]. Refined grains accumulate more grain boundaries, leading to the hindrance of dislocation slip and termination of the slip band at the grain boundaries. The difference between the strain degrees inside the refined grains and near the grain boundaries is slight, yielding a uniform deformation. Therefore, the chance of cracking due to stress concentration is reduced, and cracks are less likely to expand between the refined grains, which can improve the ductility of the joint to a certain extent. Stern et al. [40] studied the typical transition zone in ferritic stainless steel MPW joints and found that the grain size on the interface is less than 0.5 μm, with a total fine-grained transition zone width of 40 μm adjacent to the interface. These findings have also been supported by experimental results from high-velocity impact joints, suggesting that refined grains can alleviate local concentrated stresses during the cooling process [41].

As seen in Figure 9, nanocrystalline Al_2Cu phases (less than 20 nm) were confirmed to be generated by TEM analysis. The formation of Al_2Cu occurs predominantly due to highly accelerated diffusion in a very short time, which can be explained as follows: Firstly, the diffusion coefficient of Cu in Al is higher than that of Al in Cu, with the interdiffusion coefficient of Cu in Al always more

 doi:10.20944/preprints202402.0246.v1

significant than that of Al in Cu at higher temperatures [42]. These factors favor the formation of an Al-rich phase of Al_2Cu. Secondly, the activation energies for forming various Al/Cu IMCs in different temperature ranges are summarized in the literature [43–46]. The results showed that Al_2Cu is more easily created than other IMC phases in solid-state processing. Moreover, interfacial element diffusion involving thermodynamics and accelerated diffusion kinetics is required to make a diffusion layer containing Al_2Cu. As per the model developed by Pretorius et al. [47,48] that uses the adequate heat of formation (EHF), the first phase in an Al-Cu binary system could be predicted. It is expected that Al_2Cu will appear first in the diffusion zone due to the maximum negative EHF [18]. Gao et al. [49] studied the growth behavior of Al_2Cu and summarized previous studies, concluding that Al_2Cu is often dendritic and layered. Generally, the intermetallic Al_2Cu phase is characterized by high brittleness and low ductility. Due to the regular lattice structure of the intermetallic Al_2Cu phase, its essential symmetry in the bond network and the uniformity of the covalent bond distribution are poor, resulting in a shallow spatial distribution of its valence electron structure, which is an essential cause of brittleness [50]. On the other hand, the distribution of the charge density of the Al_2Cu phase is highly non-uniform, showing severe anisotropy, which leads to the inability of the Al_2Cu phase to deform during deformation. Uniform deformation and mechanical anisotropy characteristics make it difficult for dislocations to slip within the crystal, resulting in poor deformability and low ductility of the Al_2Cu phase. It is worth noting that grain refinement improved not only the material's strength but also the plasticity and ductility of the material, which is unmatched by other strengthening methods. The yield strength and grain diameter of polycrystalline materials satisfy the Hall-Pitch formula [51,52]:

$$\sigma_s = \sigma_0 + K \bullet d - 1/2$$

The equation for determining the strength of a polycrystal uses variables such as σ_0, which represents the yield strength of a single crystal metal; d is the average diameter of each grain in the polycrystal; and K characterizes how grain boundaries affect strength. The nanocrystalline Al_2Cu phase must be deformed because of differences in orientation between grains, resulting in a complex dislocation network due to more slips. In addition, improvements in mechanical properties are primarily dependent on nanosized precipitates acting as obstacles to dislocation movement, utilizing precipitation hardening. Dislocations become pinned by the precipitates and eventually either shear or bypass them during the interaction process, known as the Orowan strengthening mechanism [53]. Therefore, the finer the grains, the stronger the material because of more grain boundaries and a significant strengthening effect.

The unique and intricate interface structure can be attributed to the high-energy rate collision nature of EMPW, which occurs in an instant (40-60 μs), indicating the occurrence of high temperature, high pressure, rapid heating, and rapid cooling during the collision. This creates a confined and highly restricted environment for forming intricate structures, unlike the equilibrium process of traditional phase diagrams. The intense strain resulting from peak-to-peak collision generates instantaneous high temperature, promoting the fusion of the micro-domain interface at a nano-scale level and leading to rapid solidification. This leads to a nanocrystalline-amorphous hybrid structure (Figure 9f,k); the nanocrystalline Al_2Cu induces stress disturbances during deformation that interact with shear bands in the amorphous phase. This impedes the rapid expansion and fracture of the amorphous shear band, thereby improving the plasticity [54,55]. Song et al. [56] also found that amorphous dispersion in ultrafine grains enhances interfacial strength and plasticity. Consequently, the hybrid strengthening mechanism accounts for the higher interfacial fatigue strength of the EMPWed joint compared to that of the matrix. In addition, the impact of hybrid nanocrystalline-amorphous volume fraction on the mechanical properties and plastic deformation process is apparent. According to the mixing law of strength properties, increasing the volume fraction of crystalline phases naturally improves the overall strength of the sample [57–59]. Combining nanocrystalline with a high elastic modulus and amorphous phase with a lower elastic modulus significantly enhances the amorphous's "soft phase" strength as the nanocrystalline acts as the "hard" phase. Moreover, with the same grain size and arrangement, increasing the nanocrystalline

 doi:10.20944/preprints202402.0246.v1

volume fraction intensifies the hindering effect on shear band expansion [60]. Meanwhile, under the same volume fraction and distribution, expanding the quantity of nanocrystalline divides the amorphous matrix into smaller gaps between the crystals in space, which contributes to inhibiting nucleation and expansion of mature shear bands. Albe et al. [61] extensively explain that this division actively suppresses the nucleation of shear transition regions/immature shear bands in the amorphous matrix, reducing the number of atoms with a particular local atomic shear strain value. The nanocrystalline distribution may also influence the hindering effect of immature shear bands in the amorphous phase. Therefore, regulating the effect of nanocrystalline-amorphous hybrid strengthening deserves more in-depth studies in the future.

5. Conclusions

Electromagnetic pulse welding (EMPW) of Al6061-to-Cu dissimilar lap joints was performed at discharge voltages of 12 kV, 14 kV, and 16 kV, and the resulting fatigue properties, interfacial features, and strengthing mechanism were analyzed. The following conclusions can be drawn:

(1) The load-bearing capacity of the EMPWed Al/Cu dissimilar joints made at the discharge voltages of 14 kV and 16 kV is superior to that of 12 kV and even higher than Al base alloy due to joint failure occurred on Al base metal (BMF mode). While only interfacial failure (IF mode) happened for 12 kV joints, their failure loads were still significantly higher than those specified in the AWS D17.2 standard.

(2) Fatigue life is proportional to the tensile lap shear loads of the joints, i.e., fatigue cycles of the joint made at a discharge voltage of 14 kV are one order of magnitude higher than that of 12 kV at all loading levels except at the fatigue limit of 0.5 kN. Only the BMF mode was observed for the 14 kV joints at the highest P_{max} = 3.0 kN; IF mode occurred at other load conditions with a fatigue strength coefficient of 360 MPa and fatigue strength index of -0.2188. Meanwhile, the IF mode happened for all 12 kV joints, corresponding to 73 MPa and -0.1076. Basquin's equation indicates that when the fatigue strength coefficient is higher, and the fatigue strength index is lower, the fatigue life is longer, resulting in a more excellent fatigue resistance for the 14 kV joints than that of 12 kV.

(3) The fatigue fracture process for the EMPWed Al/Cu lap joint is that stress concentration and crack initiation occur from the outer edge of the annular welding area until joint failure. The typical "tire-mark" fatigue striation appeared on the 14 kV joint at Pmax = 1 kN and 2.5 kN. In comparison, the 12 kV joint only showed a slight fatigue or dimple feature, indicating that the 14 kV joint has higher ductility than the 12 kV and can withstand longer plastic deformation.

(4) The high EBSD acquisition was achieved except for the transition zone due to the formation of ultra-fine nanocrystalline Al2Cu phase and amorphous phase, along with many dislocations. Dense LAGBs (low-angle grain boundaries) and refined grains occurred on the Al side along the bonding interface, indicating that severe plastic deformation induced dislocations to form the substructure in such an instant (40-60 μs) during the high-velocity collision of EMPW. Meanwhile, apart from the brass texture created in the local area near the interface of the Al side, most of the area displayed a freedom texture due to the short collision time.

(5) The enhanced load-bearing capacity and fatigue resistance of the EMPWed Al/Cu lap joint are not only due to the continuous interfacial diffusion layer with a "wave-like" or "inverted hook-like" pattern but also benefit from refined grains along the interface and in the transition zone, as well as hybrid amorphous-nanocrystalline microstructure, which strengthens the joint through increasing ductility induced by fine grains and regulating amorphous or nanocrystalline phases to affect the balance between strength and ductility of the Al/Cu joint.

Author Contributions: Y.Y. (Yunqi. Yan): conceptualization, formal analysis, investigation, writing—original draft, visualization, writing—review & editing. X.S. (Xinwei. She): Methodology, Formal analysis, Validation, Review & editing. Y.R.: Investigation. H.P.: Investigation. R.Z. (Ruihao. Zhang): Investigation. P.W. (Puquan. Wang): Methodology, Formal analysis, Review & editing. X.J. (Xianquan. Jiang): Conceptualization, Methodology, Formal analysis, Supervision, Validation, Review & editing.

Funding: Please add: This research was funded by the National Natural Science Foundation of China (NSFC), grant number 51971183, and Chongqing Natural Science Foundation Joint Fund for Innovation and

Development, grant number CSTB2023NSCQ-LZX0002, and Chongqing Science and Health Joint Medical Research Project, grant number 2023QNXM049, as well as the Sichuan Regional Innovation Cooperation Project, grant number 2023YFQ0003.

Institutional Review Board Statement: Not applicable.

Informed Consent Statement: Not applicable.

Data Availability Statement: Data will be made available upon request.

Acknowledgments: Y.Q. Yan is grateful for a visiting scholar provided by Southwest University. The authors would also like to thank D.L. Chen, Q. Li, A. Machin, J. Amankrah, and R. Churaman for easy access to the laboratory facilities of Ryerson University and their assistance in the experiments.

Conflicts of Interest: The authors declare that they have no known competing financial interests or personal relationships that could have appeared to influence the work reported in this paper.

References

1. Kapil, A.; Sharma, A. Magnetic pulse welding: an efficient and environmentally friendly multi-material joining technique. *J. Clean. Prod.* **2015**, *100*, 35-58.
2. Raoelison, R.N.; Racine, D.; Zhang, Z.; Buiron, N.; Marceau, D.; Rachik, M. Magnetic pulse welding: interface of Al/Cu joint and investigation of intermetallic formation effect on the weld features. *J Manuf Process.* **2014**, *16*, 427-434.
3. Galvao, I.; Leal R.M.; Loureiro, A.; Rodrigues, D.M. Material flow in heterogeneous friction stir welding of aluminium and copper thin sheets. *Sci. Technol. Weld. Join.* **2010**, *15*, 654-660.
4. Ni, Z.L.; Yang, J.J.; Hao, Y.X.; Chen, L.F.; Li, S.; Wang, X.X.; Ye, F.X. Ultrasonic spot welding of aluminum to copper: a review. *Int. J. Adv. Manuf. Technol.* **2020**, *107*, 585-606.
5. Zhang, L.P.; Wen, J.P.; Xie, J.L.; Gou, Y.; Zhang, H.H.; Chen, Y.H.; Yin, L.M.; Zhang. L.; Gao, L.; Wang, Gang. Intermetallic compounds growth and morphology evolution of Al6061/SS304 electromagnetic pulse welding joint interface during post-weld heat treatment. *J. Mater. Res. Technol.* **2024**, *28*, 4001-4011.
6. Lee, K.J.; Kumai, S.; Arai, T.; Aizawa, T. Interfacial microstructure and strength of steel/ aluminum alloy lap joint fabricated by magnetic pressure seam welding. *Mater. Sci. Eng. A.* **2007**, *471*, 95-101.
7. Manogaran, A.P.; Manoharan, P.; Priem, D.; Marya, S.; Racineux, G. Magnetic pulse spot welding of bimetals. J *Mater Process Technol.* **2014**, *214*, 1236-44.
8. Patra, S.; Arora, K.S.; Shome, M.; Bysakh, S.; Interface characteristics and performance of magnetic pulse welded copper-steel tubes. J *Mater Process Technol.* **2017**, *245*, 278-86.
9. Mirza, F.A.; Macwan, A.; Bhole, S.D.; Chen, D.L.; Chen, X.G. Microstructure, tensile and fatigue properties of ultrasonic spot welded aluminum to galvanized high-strength low-alloy and low-carbon steel sheets. *Mater. Sci. Eng. A.* **2017**, *690*, 323-36.
10. Geng, H.H.; Xia, Z.H.; Zhang, X.; Li, G.Y.; Cui, J.J. Microstructures and mechanical properties of the welded AA5182/HC340LA joint by magnetic pulse welding, *Mater Charact.* **2018**, *138*, 229-237.
11. Yvell, K.; Grehk, T.M.; Hedström, P.; Borgenstam, A.; Engberg, G. Microstructure development in a high nickel austenitic stainless steel using EBSD during in situ tensile deformation, *Mater Charact.* **2018**, *135*, 228-237.
12. Liu, J.; Cao, B.; Yang, J.W. Texture and intermetallic compounds of the Cu/Al dissimilar joints by high power ultrasonic welding, *J Manuf Process.* **2022**, *76*, 34-45.
13. Liyakat, N.A.; Veeman, D.; Improvement of mechanical and microstructural properties of AA 5052-H32 TIG weldment using friction stir processing approach, *J. Mater. Res. Technol.* **2020**, *19*, 332-344.
14. Lee, T.; Nassiri, A.; Dittrich, T.; Vivek, A.; Daehn, G. Microstructure development in impact welding of a model system. *Scr. Mater.* **2020**, *178*, 203-206.
15. Chen, S.; Daehn, G.S.; Vivek, A.; Liu, B.; Hansen, S.R.; Huang, J.; Lin, S. Interfacial microstructures and mechanical property of vaporizing foil actuator welding of aluminum alloy to steel. *Mater. Sci. Eng. A.* **2016**, *659*, 12-21.
16. Raoelison, R.N.; Sapanathan, T.; Buiron, N.; Rachik, M. Magnetic pulse welding of Al/Al and Al/Cu metal pairs: consequences of the dissimilar combination on the interfacial behavior during the welding process. *J. Manuf. Process.* **2015**, *20*, 112-127.
17. Aws, D17.2/D17.2M Specification for Resistance Welding for Aerospace Applications, American Welding Society, Miami, FL, **2019**.
18. Wang, P.Q.; Chen, D.L.; Ran, Y.; Yan, Y.Q.; She, X.W.; Peng, H.; Jiang, X.Q. Electromagnetic pulse welding of Al/Cu dissimilar materials: Microstructure and tensile properties. *Mater. Sci. Eng. A.* **2020**, *792*, 139842.
19. Wang, P.Q.; Chen, D.L.; Ran, Y.; Yan, Y.Q.; Peng, H.; Jiang, X.Q. Fracture characteristics and analysis in dissimilar Cu-Al alloy joints formed via electromagnetic pulse welding. Materials (Basel). **2019**, *12*, 3368.

20. Mirza, F.A.; Macwan, A.; Bhole, S.D.; Chen, D.L.; Chen, X.G. Microstructure, tensile and fatigue properties of ultrasonic spot welded aluminum to galvanized high-strength-low-alloy and low-carbon steel sheets. *Mater. Sci. Eng. A*. **2017**, *690*, 323-336.
21. Feng, A.H.; Chen, D.L.; Ma, Z.Y. Microstructure and Low-Cycle Fatigue of a Friction-Stir-Welded 6061 Aluminum Alloy. *Metall. Mater. Trans. A*. **2010**, *41*, 2626-2641.
22. Mohammed, S.M.A.K.; Dash, S.S.; Jiang, X.Q.; Li, D.Y.; Chen, D.L. Ultrasonic spot welding of 5182 aluminum alloy: Evolution of microstructure and mechanical properties. *Mater. Sci. Eng. A*. **2019**, *756*, 417-429.
23. Liu, M.; Zou, T.F.; Wang, Q.Y.; Jiang, Y.Q.; Wu, Hao.; Pei, Y.B.; Zhang, H.; Liu, Y.J.; Wang, Q.Y. Microstructure evolution, failure mechanism and life prediction of additively manufactured Inconel 625 superalloy with comparable low cycle fatigue performance, *Int J Fatigue.* **2024**, *181*, 108142.
24. Basquin, O.H. The Exponential Law of Endurance Tests. Proceedings of the American Society for testing and Materials. **1910**, *10*, 625-630.
25. Patel. V.K.; Bhole, S.D.; Chen, D.L. Fatigue life estimation of ultrasonic spot welded Mg alloy joints. *Mater. Des*. **2014**, *62*, 124-132.
26. Russell, A.M. and Lee, K.L. Structure-property relations in nonferrous metals, John Wiley & Sons, Inc., New York, NY, **2005**, 69-75.
27. Laird, C. "The influence of metallurgical structure on the mechanisms of fatigue crack propagation," in: fatigue crack propagation, ASTM STP N 415, Philadelphia, **1967**, 131-168.
28. Zhilyaev, A.P.; Swaminathan, S.; Gimazov, A.A.; McNelley, T.R.; Langdon T.G. An evaluation of microstructure and microhardness in copper subjected to ultra-high strains. *J Mater Sci.* **2008**, *43*, 7451-7456.
29. Zhang, H.; Ke, X. J.; Zhang, J. L.; Liu, J.P. Microstructure and mechanical properties investigations of copper-steel composite fabricated by explosive welding, *Mater. Sci. Eng. A*. **2018**, *731*, 278-287.
30. Peng, H.; Chen, D.L.; Guo, S.F.; Hong, H.; Zheng, K.H.; Bai, X.F.; Li, D.Y.; Jiang, X.Q. Dissimilar ultrasonic spot welding of rare-earth containing ZEK100 magnesium-to-aluminum alloy with a zinc interlayer: Microstructural evolution and mechanical properties. *J Manuf Process*. **2023**, *92*, 422-434.
31. Paul, H.; Litynska-Dobrzynska, L.; Prazmowski, M. Microstructure and phase constitution near the interface of explosively welded aluminum/copper plates, *Metall. Mater. Trans. A*. **2013**, *44*, 3836-3851.
32. Liyakat, N.A.; Veeman, D. Improvement of mechanical and microstructural properties of AA 5052-H32 TIG weldment using friction stir processing approach. *J. Mater. Res. Technol.* **2022**, *19*, 332-344.
33. Li, S.C.; Guo, C.Y.; Hao, L.L. In-situ EBSD study of deformation behavior of 600 MPa grade dual-phase steel during uniaxial tensile tests, *Mater. Sci. Eng. A*. **2019**, *759*, 624-632.
34. Stern, A.; Shribman, V.; Ben-Artzy, A. Interface phenomena and bonding mechanism in magnetic pulse welding. *J. Mater. Eng. Perform.* **2014**, *23*, 3449-3458.
35. Lu, H.W.; Ye, F.X.; Wang, Y.H. Orthogonal experiments and bonding analysis of ultrasonic welded multi-strand single core copper cables, *J Manuf Process.* **2022**, *78*, 1-10.
36. Liu, J.; Cao, B.; Yang, J.W. Texture and intermetallic compounds of the Cu/Al dissimilar joints by high power ultrasonic welding, *J Manuf Process.* **2022**, *76*, 34-45.
37. Gholinia, A.; Humphreys, F.; Prangnell P.B. Production of ultra-fine grain microstructures in Al-Mg alloys by conventional rolling. *Acta Mater.* **2002**, *50*, 4461-4476.
38. Trueb, L. Electron-microscope study of thermal recovery processes in explosion-shocked nickel. *J. Appl. Phys.* **1969**, *40*, 2976-2987.
39. Wright, R.N.; Mikkola, D.E. Deformation twinning: time dependence and associated strengthening effects in shock-loaded Cu-8.7at.%Ge. *Mater. Sci. Eng. A*. **1982**, *53*, 273-283.
40. A. Stern, M. Aizenshtein, Bonding zone formation in magnetic pulse welds. *Sci. Technol. Weld. Join.* **2002**, *7*, 339-342.
41. Dudas, J.H.; Collins, F.R. Preventing weld cracks in high-strength aluminum alloys. *Weld J*, **1966**, *45*.
42. Xu, J. Study on process and properties of welding joint of aluminum-copper dissimilar metals welding-brazing, Master's Thesis, Lanzhou University of Science and Technology, China, **2015**.
43. Chen, C.Y.; Hwang, W.S. Effect of annealing on the interfacial structure of aluminum-copper joints. *Mater. Trans.* **2007**, *48*, 1938-1947.
44. Lee, W.B.; Bang, K.S.; Jung, S.B. Effects of intermetallic compound on the electrical and mechanical properties of friction welded Cu/Al bimetallic joints during annealing. *J. Alloys Compd.* **2005**, *390*, 212-219.
45. Amani, H.; Soltanieh, M. Intermetallic phase formation in explosively welded Al/Cu bimetals. *Metall. Mater. Trans. B*. **2016**, *47*, 2524-2534.
46. Guo, Y.J.; Liu, G.W.; Jin, H.Y.; Shi, Z.Q.; Qiao, G.J. Intermetallic phase formation in diffusion-bonded Cu/Al laminates. *J. Mater. Sci.* **2011**, *46*, 2467-2473.
47. Pretorius, R.; Marais, T.K.; Theron, C.C. Thin film compound phase formation sequence: an effective heat of formation model. *Mater. Sci. Rep*. **1993**, *10*, 1-83.

48. Pretorius, R.; Vredenberg, A.M.; Saris, F.W.; Reus, R.D. Prediction of phase formation sequence and phase stability in binary metal-aluminum thin-film systems using the effective heat of formation rule. *J. Appl. Phys.* **1991**, *70*, 3636-3646.
49. Gao, K. Study on growth morphology, orientation and mechanical properties of Al_2Cu phase of directionally solidified intermetallic compounds. PhD's Thesis, Northwestern Polytechnical University, China, **2014**.
50. Zhi, W. Brittle criterion for valence electron structure of intermetallic compounds. *J. China Ordnance.* **2001**, *22*, 248-251.
51. Hall, E.Q. The deformation and ageing of mild steel: III discussion of results. Proceedings of the Physical Society of London Section B. **1951**, *64*, 747-753.
52. Petch, N.J. The cleavage strength of polycrystals. *J. Iron Steel Res.* **1953**, *174*, 25-58.
53. Sun, G.P.; Lei, M.Y.; Liu, S.; Wen, B. Orowan strengthening with consideration of thermal activation. *COMP MATER SCI*. **2024**, *233*, 112720.
54. Ashby, M.; Greer, A. Metallic glasses as structural materials. *Scr. Mater.* **2006**, *54*, 321-326.
55. Song, W.L.; Song, K.K. Phase change ductile plasticization of amorphous alloys. *Prog. Mater. Sci.* **2014**, *33*, 300-310.
56. Song, K.K.; Pauly, S.; Sun, B.A.; Tan, J.; Stoica, M. Correlation between the microstructures and the deformation mechanisms of CuZr-based bulk metallic glass composites. *AIP Advances.* **2013**, *3*, 012116.
57. Hofmann, D.C.; Suh, J.Y.; Wiest, A.; Duan, G.; Lind, M.L.; Demetriou, M.D.; Johnson, W.L. Designing metallic glass matrix composites with high toughness and tensile ductility. *Nature.* **2008**, *451*, 1085-1089.
58. Wu, Y.; Xiao, Y.H.; Chen, G.L.; Liu, C.T.; Lu, Z.P. Bulk metallic glass composites with transformation-mediated work-hardening and ductility. *Adv. Mater.* **2010**, *22*, 2770-2773.
59. Pauly, S.; Gorantla, S.; Wang, G.; Kuhn, U.; Eckert, J. Transformation-mediated ductility in CuZr-based bulk metallic glasses. *Nat. Mater.* **2010**, *10*, 1038.
60. Zhou, H.F.; Qu, S.Q.; Yang, W. An atomistic investigation of structural evolution in metallic glass matrix composites. *Int. J. Plast.* **2013**, *44*, 147-160.
61. Albe, K.; Ritter, Y.; Daniel, S. Enhancing the plasticity of metallic glasses: shear band formation, nanocomposites and nanoglasses investigated by molecular dynamics simulations. *Mech. Mater.* **2013**, *67*, 94-103.